Tensile, Fatigue, and Creep Properties of Aluminum Heat Exchanger Tube Alloys for Temperatures from 293 K to 573 K (20 °C to 300 °C)

SÖREN KAHL, HANS-ERIK EKSTRÖM, and JESUS MENDOZA

Since automotive heat exchangers are operated at varying temperatures and under varying pressures, both static and dynamic mechanical properties should be known at different temperatures. Tubes are the most critical part of the most heat exchangers made from aluminum brazing sheet. We present tensile test, stress amplitude-fatigue life, and creep–rupture data of six AA3XXX series tube alloys after simulated brazing for temperatures ranging from 293 K to 573 K (20 °C to 300 °C). While correlations between several mechanical properties are strong, ranking of alloys according to one property cannot be safely deduced from the known ranking according to another property. The relative reduction in creep strength with increasing temperature is very similar for all six alloys, but the general trends are also strong with respect to tensile and fatigue properties; an exception is one alloy that exhibits strong Mg-Si precipitation activity during fatigue testing at elevated temperatures. Interrupted fatigue tests indicated that the crack growth time is negligible compared to the crack initiation time. Fatigue lifetimes are reduced by creep processes for temperatures above approximately 423 K (150 °C). When mechanical properties were measured at several temperatures, interpolation to other temperatures within the same temperature range was possible in most cases, using simple and well-established equations.

DOI: 10.1007/s11661-013-2003-5

I. INTRODUCTION

MOST automotive heat exchangers are today made from aluminum sheet. Operating pressures and temperatures have been increasing while material thicknesses have been decreasing. This is a continuous development motivated by the task to reduce vehicle weight and toxic emissions and to improve fuel efficiency.

Today, it is often more challenging to fulfill the requirements on mechanical durability than the functional requirements on heat transfer. This is especially true for applications such as charge air coolers for heavy vehicles, but the durability requirements for other types of automotive heat exchangers have also become more demanding.

Radiators operate at around 373 K (100 °C) and at pressures of up to 250 kPa, while charge air coolers for heavy vehicles can be subjected to operating temperatures of up to 548 K (275 °C) and pressures of up to 350 kPa. Typical durability tests during product development include thermal cycling, pressure cycling, and vibration tests. During service life, particularly charge air coolers are also subjected to high loads at high temperatures for long times, probably of the order of 1 month accumulated over the total lifetime of the vehicle.

In principle, it is possible to achieve all current durability requirements with standard heat exchanger alloys through the proper design of the heat exchanger and correct choice of the material thickness. More advanced alloys with better mechanical properties, on the other hand, allow for reduced material thickness. Sometimes, the situation may occur where the change to a stronger alloy makes it possible to meet increased durability requirements without a design change.

On the material level, it is the fatigue and creep properties of the material that are most relevant for heat exchanger durability. Load spectra and temperatures vary strongly between different types of heat exchangers, but material characterization must be limited to a few generic tests in order to keep the scope and costs of testing within manageable proportions. We consider constant-amplitude strain-controlled low-cycle fatigue tests, stress-controlled high-cycle fatigue tests, and creep rupture tests as most relevant.

AA3XXX series alloys are the most common heat exchanger tube materials. They are usually roll-plated with a lower-melting silicon-containing AA4XXX series alloy that melts during the brazing process of heat exchanger manufacture and forms the joints between the different parts of the heat exchanger. Plating alloys are often called clad alloys in order to distinguish them from the center material that is often called core alloy. Besides

SÖREN KAHL, Manager, is with the Sapa Heat Transfer Technology, Finspong, Sweden, and also Visiting Researcher with the Division of Engineering Materials, Linköping University, Linköping, Sweden. Contact e-mail: soren.kahl@sapagroup.com HANS-ERIK EKSTRÖM, Consultant, and JESUS MENDOZA, Manager, are with the Sapa Technology, Finspong, Sweden.

Manuscript submitted June 10, 2013.
Article published online September 25, 2013

clad alloys used as braze alloys, there are also clad alloys that offer anodic corrosion protection to the core alloy.

Manganese is the main alloying element of the AA3XXX core alloys; it assures a large grain-size and increases the mechanical strength by both solid solution and dispersoid strengthening. Sometimes, Mg is added in small concentrations and increases the strength by solution hardening, or—in combination with Si—by precipitation hardening. Another common alloying element is Cu that mainly contributes to strength by solid solution hardening. All alloying elements influence other material properties as well, for example thermal conductivity and corrosion behavior. A general description of AA3XXX series alloys for heat exchangers can be found elsewhere.[1]

During the brazing process of heat exchanger manufacture, the materials become very soft since they are kept at around 873 K (600 °C) for several minutes. Strength contributions from strain hardening and grain boundaries are removed and the solid solution levels of many alloying elements increase substantially during brazing. It is the material properties after brazing that are relevant for heat exchanger durability; therefore, we have performed all material characterization after a heat treatment that shall simulate the industrial brazing process.

The most critical heat exchanger materials with respect to durability are the materials used for the tubes: Tubes are prone to failure and a leak in a tube constitutes a failure of the complete heat exchanger. Material properties after brazing are influenced by all steps of production, including the last cold rolling steps. Tube materials are typically in the thickness range from 0.2 to 0.5 mm, which makes several types of mechanical tests rather difficult. This applies particularly to strain-controlled fatigue tests at elevated temperatures. To the best of our knowledge, these tests have not yet been performed on tube material in the final thickness, and we could not yet acquire such data either.

We have systematically collected tensile test data, stress amplitude-fatigue life data, and creep data at different temperatures. Strain-controlled low-cycle fatigue tests have so far not been possible for our thin and soft material because mechanical extensometers cannot be used. Data have been collected for a braze-clad AA3003 reference alloy as well as for more advanced heat exchanger tube alloys.

An abundance of fatigue data exists for other aluminum alloy systems.[2] However, little data have so far been published on the fatigue and creep properties of wrought AA3XXX series alloys for heat exchanger applications.[3–9]

The combined analysis of tensile, fatigue, and creep data presented in this article is much more comprehensive than what have previously been published. Nevertheless, since mechanical tests at elevated temperatures are rather expensive, it is important to find possibilities to predict material behavior at temperatures where data do not exist. We have therefore examined the measured data with the intention to identify general tendencies that make predictions possible.

II. PROCEDURE AND MATERIAL

The core alloys and clad layers of the materials of this investigation are given in Table I. The braze alloys were AA4XXX series alloys with a solidus temperature of 850 K (577 °C), which is well below the brazing temperature of around 873 K (600 °C). All materials were produced and supplied by Sapa Heat Transfer. The common process steps involved packaging of the core layer ingot and the clad layer plates, preheating of the package, hot rolling of

Table I. Core Alloy and Clad Layer Compositions in Weight Percentage

Alloy	Thickness (mm)	Clad Layers	Si	Fe	Cu	Mn	Mg	Zr	Zn	Ti
Core alloys										
AA3003	0.40	AA4343 10 pct, 2-side	0.12	0.51	0.11	1.06	—	—	—	0.05
Alloy-A	0.27	AA4045 10 pct, 2-side	0.07	0.21	0.83	1.70	—	0.13	—	—
Alloy-B	0.485	AA4343 10 pct, 2-side	0.06	0.22	0.29	1.08	0.22	—	—	0.02
Alloy-C	0.25	AA4343 10 pct, 2-side	0.06	0.20	0.64	1.70	0.05	0.13	—	0.04
Alloy-D	0.42	AA4343 10 pct, 2-side	0.06	0.19	0.82	1.62	0.22	0.12	—	0.07
Alloy-E	0.35	AA4343 10 pct, 1-side FA6815 5 pct, 1-side	0.71	0.28	0.27	0.53	0.29	—	—	0.14
Clad layer alloys										
AA4343	clad layer	—	8	0.15	—	—	—	—	—	—
AA4045	clad layer	—	10	0.15	—	—	—	—	—	—
FA6815	clad layer	—	0.82	0.20	—	1.65	—	0.13	1.5	

Concentrations below 0.01 wt pct have been excluded. Clad layer thicknesses are given relative to total material thicknesses. One- or double-side cladding is indicated. For the case of double-side cladding, each of the two clad layers has the given thickness. Clad layer compositions are typical values.

the package and coiling of the sheet, cold to the final thickness, and final annealing to temper H24.

The first part of hot rolling was performed by a reversible break down mill, from a package thickness between 550 and 600 mm down to between 15 and 20 mm thickness. Afterward, the material was rolled down to approximately 4 mm thickness in a tandem hot mill. Cold rolling was performed on two different cold rolling mills, where the material was transferred from the first to the second cold rolling mill at a thickness of approximately 0.8 mm.

Tensile, fatigue, and creep tests were performed on material in the delivery gage, between 0.2 and 0.5 mm for heat exchanger tube alloys; the only exceptions were a few of the creep tests, which were performed on unclad material in 0.9 mm thickness. We took all samples directly from the production plant since surface quality and thickness homogeneity of industrially rolled material are better than for laboratory rolled material. For the data presented in this article, we have not found any indications that the temperature dependence of the mechanical properties changed with material thickness.

All material was subjected to simulated brazing before specimens were prepared. The simulated brazing consisted of heating to 873 K (600 °C) during 20 minutes under a controlled nitrogen gas atmosphere, 5 minutes dwell time at 873 K (600 °C), and subsequent fast cooling in air. Material was mounted inside the furnace with the sheet plane parallel to the direction of gravity and the rolling direction parallel to the horizontal direction. Molten braze metal flowed toward the bottom of the sheet and accumulated there during the simulated brazing; no specimens were taken from this bottom part.

Two alloys assume a special role in this study: (1) AA3003 serves as a reference and example alloy; AA3003 has the lowest mechanical strength among the alloys of the present investigation. This alloy was roll-plated on each side with an AA4343 braze alloy that had—on each side of the AA3003 core alloy—a thickness of 10 pct of the total material thickness. (2) Alloy-A, roll-plated on each side with an AA4045 braze alloy of 10 pct of the total material thickness, was the alloy chosen for several selected investigations.

Chemical composition was determined by optical emission spectroscopy. For tensile tests discussed in this article, specimens were extracted parallel to the rolling direction. The extensometer gage length was 50 mm for all tensile tests. Fatigue and creep test specimens were also extracted parallel to the rolling direction. All specimens were milled out; the milled edges of the fatigue test specimens were subsequently ground and polished.

Tensile tests at room temperature were performed according to ISO 6892-1:2009. Yield strength and proof stress are used as synonyms in this text while we actually measured the 0.2 pct proof stress values, $R_{p0.2}$. Tensile test specimens for yield strength determination of braze-simulated material should have a parallel section of reduced width that is longer than the minimum length of 75 mm recommended by ISO 6892-1:2009; this issue will be discussed in Section III–B. We performed all yield strength measurements on specimens that were 12 mm wide and had parallel edges over their complete length of 215 mm between the upper and lower grip of the tensile test device.

The height of the specimen surface shown in Figure 2(b) was measured with an optical measurement microscope along two lines perpendicular to the milled edges.

For elevated-temperature tensile tests up to 573 K (300 °C), the specimens were heated by a direct electric current. The target temperature was regulated *via* an adhesive thin-wire thermocouple in the specimen center, and the temperature uniformity was monitored by two additional thermocouples positioned 20 mm below and above the specimen center. The temperature was highest in the center of the specimen and decreased by a maximum of 3 K (3 °C) to the thermocouple positions at 20 mm above and below the specimen center. Temperature overshooting during heating was below 4 K (4 °C). After the yield strengths had been reached, the tests were performed with constant crosshead speeds such that strain rates roughly varied between 1.5×10^{-3} s^{-1} at the start and 3.3×10^{-3} s^{-1} at the end of the test. The main advantages of this setup were the short times required for heating and cooling of the specimens.

A few tensile tests were also performed with specimen and grips placed inside a convection furnace. In this case, dog-bone-shaped specimens according to ISO 6892-1:2009 with a parallel length of 75 mm were used. The temperature uniformity was within ±1 K (±1 °C).

Axial stress-controlled fatigue tests were performed on flat specimens with parallel sections of reduced width of 20 mm length and 15 mm width. The load ratio was $R = 0.1$. Testing devices were servo-hydraulic and operated at 27 to 30 Hz; the applied load varied sinusoidically. Before start of the test, the specimens were kept for 30 minutes at the testing temperature. During testing, temperature variation over the specimen section of reduced width was smaller than ±5 K (±5 °C).

The specimens for creep rupture tests possessed parallel gage sections of 80 or 120 mm length and 20 mm width. The specimen grip sections contained center holes where the specimens were pinned to adapters. Before start of the creep test, specimens were held 16 to 20 hours at testing temperature. During testing, temperature variations with time were regulated to within ±3 K (±3 °C) over the gage length for temperatures up to 573 K (300 °C). All tests were progressed at constant force to final rupture.

Tensile tests were performed by Sapa Technology, Sweden and China, fatigue tests by Exova, Sweden, and Technical University Clausthal, Germany, and creep tests by Siemens Industrial Turbomachinery, Sweden, and Swerea KIMAB, Sweden. Regression analyses and calculations were carried out with the software R.[10,11]

III. RESULTS AND DISCUSSION

A. *Correlations Between Results from Different Mechanical Tests*

Relations between testing temperature and various mechanical quantities are shown in Figure 1. The latter include proof strength $R_{p0.2}$, tensile strength R_m, fatigue

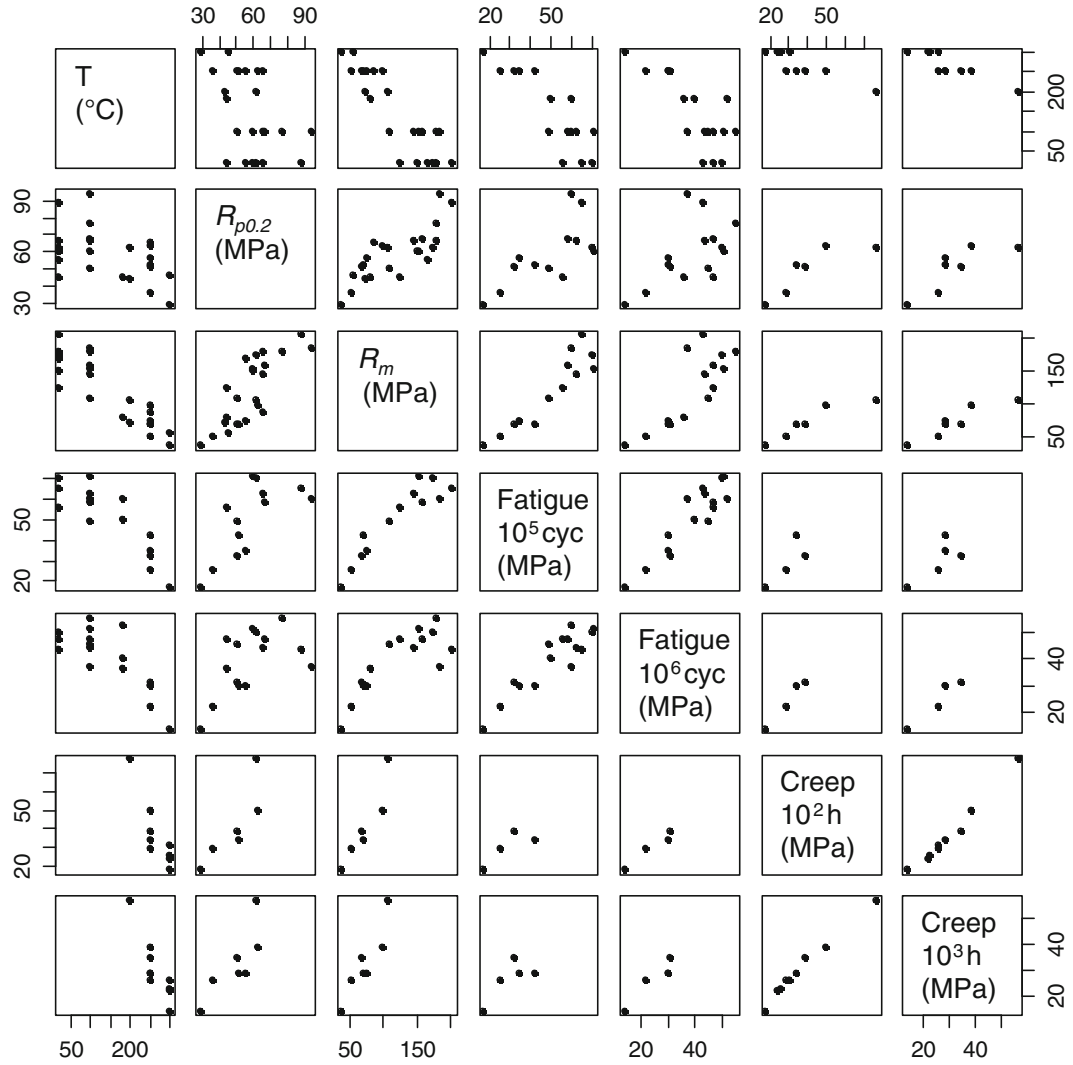

Fig. 1—Relations between results from different mechanical tests. If two quantities were measured for the same alloy at the same temperature, this resulted in one point in each of the two respective plots. Fatigue strength is given in terms of stress amplitude for the indicated number of cycles, creep strength in terms of creep rupture stress for the indicated number of hours.

Table II. Pearson Correlation Coefficients for the Data Shown in Fig. 1

	$R_{p0.2}$ (MPa)	R_m (MPa)	Fatigue 10^5 cyc (MPa)	Fatigue 10^6 cyc (MPa)	Creep 10^2 h (MPa)	Creep 10^3 h (MPa)
$R_{p0.2}$ (MPa)	1	0.80	0.71	0.56	0.84	0.81
R_m (MPa)	0.80	1	0.92	0.81	0.94	0.93
Fatigue, 10^5 cycles (MPa)	0.71	0.92	1	0.92	0.81	0.77
Fatigue, 10^6 cycles (MPa)	0.56	0.81	0.92	1	0.98	0.94
Creep, 10^2 h (MPa)	0.84	0.94	0.81	0.98	1	0.99
Creep, 10^3 h (MPa)	0.81	0.93	0.77	0.94	0.99	1

stress amplitude for failure after 10^5 and 10^6 cycles, and creep rupture stress at 10^2 and 10^3 hours to rupture.

Each relation between two quantities is shown by two diagrams, where the axes are exchanged. If two quantities were measured for the same alloy at the same test temperature, this contributed one data point in each of the two diagrams. Not all mechanical tests were carried out on all alloys at the same test temperatures; therefore, the numbers of data points differ between diagrams.

In most cases, where two quantities appear to be correlated, the correlations seem to be close to linear. Therefore, we supplemented the graphical information provided by Figure 1 with Pearson correlation coefficients, which are given in Table II.

The following quantities have correlation coefficients between 0.9 and 1.0 and are thus strongly correlated: Tensile strength to fatigue strength after 10^5 cycles, and to creep strength after both 10^2 and 10^3 hours; fatigue

strength after 10^6 cycles to fatigue strength after 10^5 cycles and to creep strength after both 10^2 and 10^3 hours.

These results should only be understood as tendencies and must not be misinterpreted in such a way that for example the alloy that ranks highest for a certain of these strongly correlated quantities at a certain test temperature also ranks highest for the other quantities at the same test temperature. In other words, substantial differences in ranking of heat exchanger tube alloys with respect to different mechanical properties are not ruled out by these high correlation coefficients. An example will be given later in this article.

The correlations have been calculated for the alloys given in Table I and it cannot be tacitly assumed without further investigations that very similar correlations are also valid for other heat exchanger alloys. On the other hand, the present investigation is rather general in the sense that large ranges of tensile and fatigue strengths are covered by the alloys and testing temperatures. The range of creep rupture strength is smaller because creep only becomes significant at elevated temperatures.

B. *Tensile Test Results*

We obtained 2 to 6 MPa lower values of room temperature yield strength on specimens with dog-bone shape and 75 mm length of the parallel section of reduced width according to ISO 6892-1:2009 than on specimens with parallel edges over the complete specimen length. These braze-simulated tube material specimens often developed a slight curvature transverse to the load direction.

The comparatively strong curvature of an Alloy-D specimen after fracture is shown in Figure 2. The fracture surface is displayed in Figure 2(a). The height of the specimen surface along two lines perpendicular to the milled specimen edges is depicted in Figure 2(b); the height measurements were performed approximately 70 mm away from the fracture surface since the measured curvature should not be influenced by release of residual stresses close to the fracture. The height values scatter significantly because the braze alloy melted and re-solidified during the simulated brazing, a process that generated a rough surface. The specimen curvature is approximately described by the circular arc that is drawn as a solid line in Figure 2(b).

Such transverse curvature could be caused by through-thickness variations of the r-values of the tube materials after simulated brazing. The parallel section of 75 mm length of the dog-bone shaped specimen was probably too short for this type of material: Due to the transverse curvature, some local plastic deformation probably occurred within the 50-mm-gage length during the measurement of $R_{p0.2}$, in addition to the desired uniform 0.2 pct of plastic deformation. For strains above approximately 1 pct, the stress strain curves of dog-bone shaped specimens and specimens with parallel edges over their complete length were virtually identical.

The tensile test results for our reference alloy AA3003 are presented in Figure 3. The yield strength showed a small increase from room temperature to 373 K (100 °C) and a subsequent mild decrease with increasing temperatures. The increase in yield strength from room temperature to 373 K (100 °C) was observed for all investigated heat exchanger tube materials as shown in Figure 4(a) and is significant with respect to the experimental error.

This increase in yield strength might be caused by a precipitation or clustering reaction taking place at 373 K (100 °C), and this reaction might require the 0.2 pct plastic deformation involved in the determination of the proof stress. The holding time at 373 K

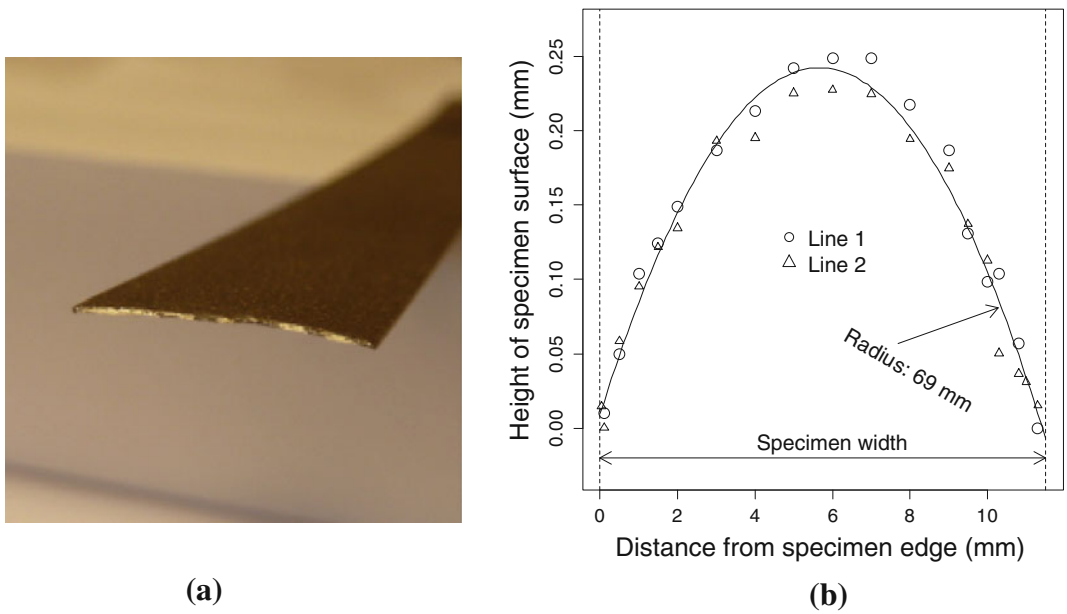

Fig. 2—Transverse curvature of an Alloy-D tensile test specimen after fracture. (*a*) View of the fracture surface. (*b*) Height profile along two lines at 70 mm distance from the fracture surface; the solid line represents a circular arc that was fitted to the data.

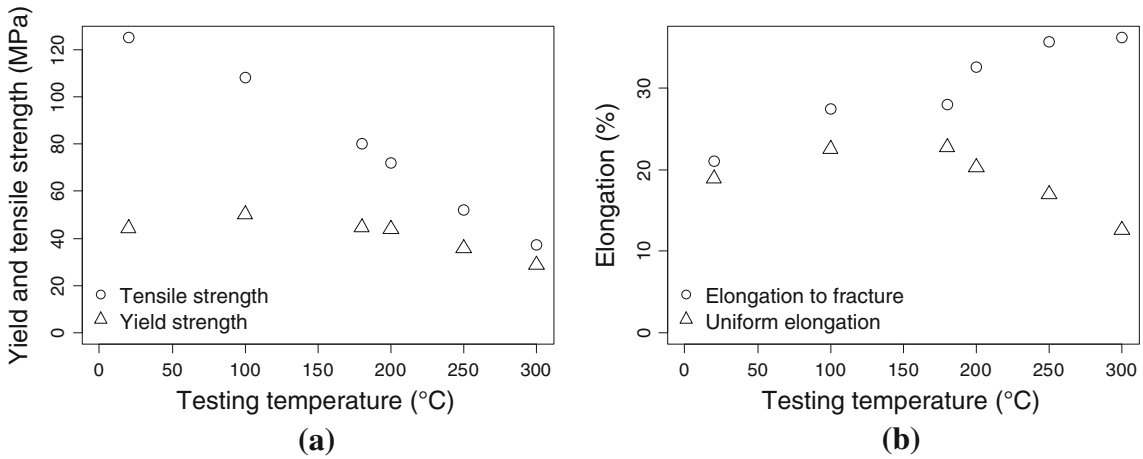

Fig. 3—Tensile test properties of 0.40-mm-thick braze-simulated, braze-clad AA3003 heat exchanger tube alloy at different temperatures.

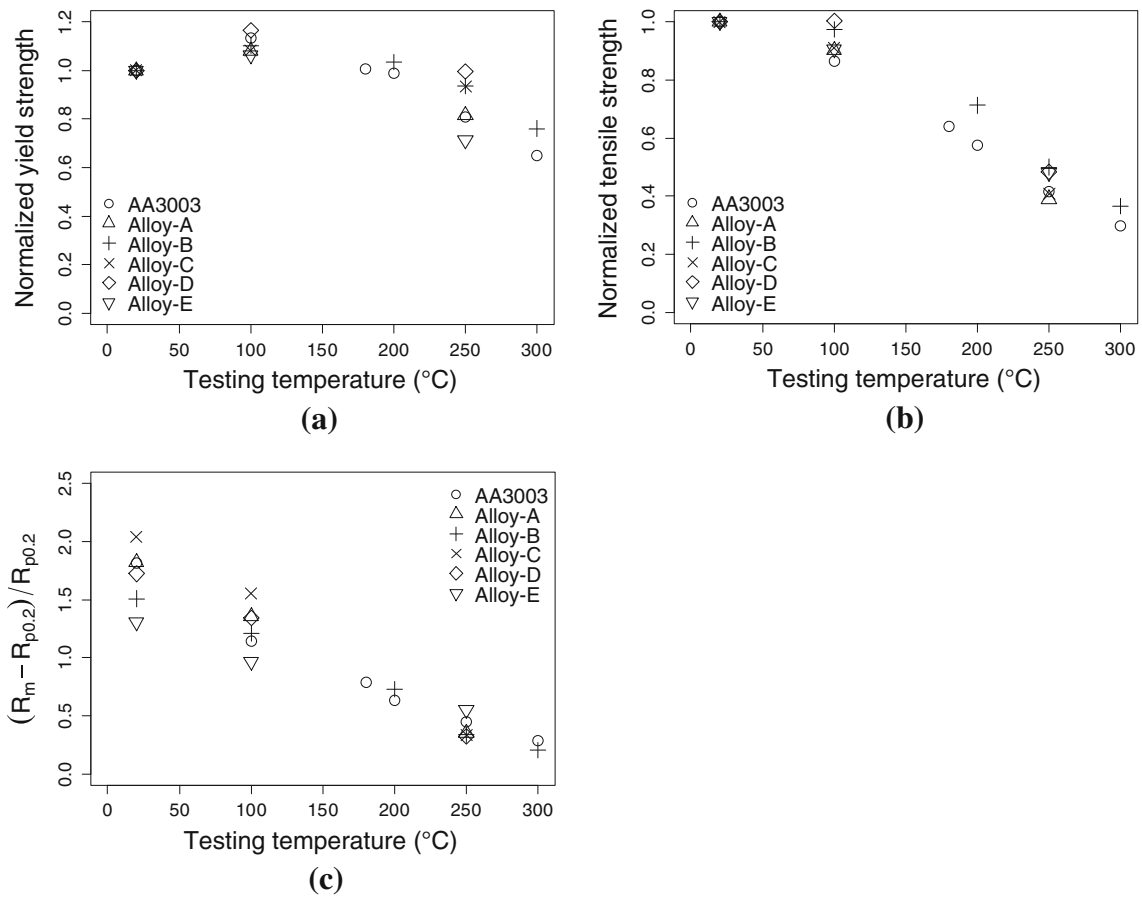

Fig. 4—(*a*) Yield strength normalized to the respective value at 293 K (20 °C). (*b*) Tensile strength normalized to the respective value at 293 K (20 °C). (*c*) Total strain hardening relative to yield strength. All quantities are given as functions of testing temperature for the six heat exchanger tube alloys presented in Table I.

(100 °C) prior to the tensile test at 373 K (100 °C) was between 3 and 5 minutes. Static pre-heating for 5 or 10 minutes at 373 K (100 °C) prior to a tensile test at room temperature did not have any influence on the yield strength of AA3003. At the present time, we would not like to speculate on further details of this strengthening mechanism.

The tensile strength decreased strongly with increasing temperature, which means that the strain hardening of the material is strongly reduced at elevated temperatures. This was true for all investigated heat exchanger tube materials, and it is in fact the behavior that is generally expected for fcc metals.[12] Tensile strength and the ratio of $R_m - R_{p0.2}$ to $R_{p0.2}$, which represents the

total strain hardening relative to the yield strength, are plotted *vs* temperature for six heat exchanger tube alloys after braze simulation in Figures 4(b) and (c).

When the average strain rate after the yield strength was increased from 6.5×10^{-4} s^{-1} to 2.5×10^{-3} s^{-1} for Alloy-A at 473 K (200 °C), we observed a 13 pct increase in measured tensile strength at approximately the same uniform strain, $A_g = 10$ pct. From the equation $\sigma = K\dot{\varepsilon}^m$, where σ is true stress, $\dot{\varepsilon}$ true strain rate, K a constant, and m the strain rate sensitivity, m can be estimated as

$$m = \frac{\ln(\sigma_1/\sigma_2)}{\ln(\dot{\varepsilon}_1/\dot{\varepsilon}_2)}. \quad [1]$$

Since typical specimen-to-specimen variations of the measured tensile strength for this material were below 2 pct, we estimated a strain rate sensitivity value between 0.08 and 0.10. This single result already indicates that comparisons of tensile test data from different heat exchanger tube alloys for temperatures above 473 K (200 °C) are only meaningful if the tests are performed with the same or at least similar strain rates.

By hot compression testing at 473 K (200 °C), strain rate sensitivities of $m = 0.04$ for pure aluminum and $m = 0.055$ for over-aged $AlMg_{0.53}Si_{0.56}$ were obtained by Blaz and Evangelista.[13] For hot torsion tests performed on AA6061, $m \approx 0.05$ at 473 K (200 °C) and $m \approx 0.08$ at 573 K (300 °C) were reported by Semiatin *et al.*[14] From tensile tests, Abedrabbo *et al.*[15] reported $m = 0.045$ at 477 K (204 °C) and $m = 0.080$ at 533 K (260 °C) for AA3003-H111. From the data of Reference 16, we calculated $m = 0.115$ for AA3103 and $m = 0.071$ for pure aluminum at 623 K (350 °C). These results indicate that both temperature and type of alloy significantly influence the reported values. The microstructure of our Alloy-A is characterized by a high density of Al-Mn-Si dispersoids and high levels of manganese in solid solution. It was shown that a high number-density of dispersoids lead to dense dislocation networks during tensile test deformation of an AA3XXX alloy.[17] The high density of dispersoids increased both the strain hardening at low strains and dynamic recovery. Therefore, we believe that the high strain rate sensitivity measured in Alloy-A is due to a high density of dispersoids.

Elongation to fracture increased with higher temperatures whereas uniform elongation reached a maximum between 373 K and 473 K (100 °C and 200 °C), as shown in Figure 3(b). We also measured low uniform elongations when we performed tensile tests at elevated temperatures in the setup with convection furnace where the temperature uniformity was virtually perfect; therefore, we do not believe that the small temperature gradient in the testing setup with resistive heating was responsible for the low uniform elongations.

Two types of necking are well known for flat specimens of rectangular cross-section: diffuse necking where the extension of the neck in the load direction is often similar to the specimen width and localized necking where the extension of the neck is often similar to the specimen thickness.[12,18] The onset of necking may be delayed by two main mechanisms, strain hardening and strain rate hardening.

Our results mean that diffuse necking started early whereas localized necking was strongly delayed during the tensile test at elevated temperatures. The onset of diffuse necking was facilitated by the reduction in strain hardening with increasing temperature, shown in Figure 4(c). Localized necking, but not diffuse necking, was delayed by strain rate hardening at elevated temperatures, as explained in the following.

Localized necking causes a local increase in strain rate by a factor of 100 when the extension of the local neck is equal to the specimen thickness.[18] The formation of a diffuse neck, on the other hand, only increases the strain rate by a factor of 8 when the extension of the local neck is equal to the specimen width.[18] For $m \approx 0.08$, the flow stress would be required to increase by 45 pct in order to form a local neck as compared to an increase by 18 pct that would be required in order to form a diffuse neck of extension equal to specimen width. The diffuse necks that lead to the low values of uniform elongations at 523 K (250 °C), however, were wider than twice the specimen width, as shown in Figure 5. Therefore, these diffuse necks only resulted in small strain rate increases as compared to the strain rate increases in local necks. We thus believe that strain rate hardening significantly delayed the formation of local necks, but not of diffuse necks.

In the following, we present an expression that is well suited to describe the true stress–true strain curves of our alloy AA3003 after braze simulation. In the Bergström model,[19] the true stress–true strain σ–ε curve has been derived from the well-known relation[20]

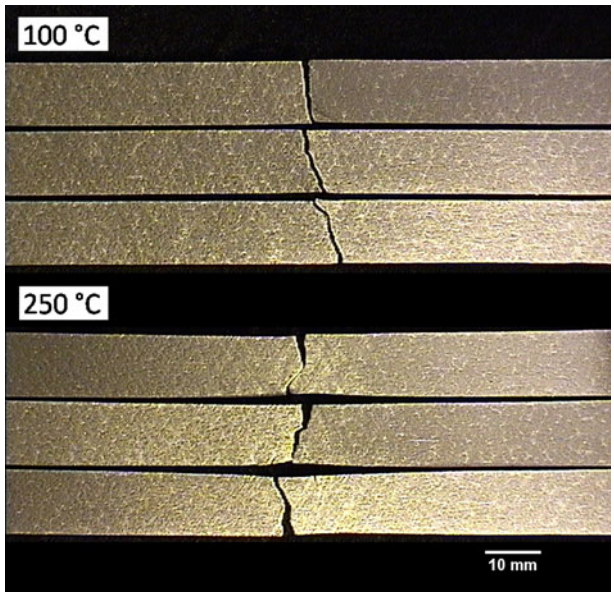

Fig. 5—Fracture zones of AA3003 tensile test specimens after testing at 373 K and 523 K (100 °C and 250 °C).

$$\sigma(\varepsilon) = \sigma_0 + \alpha G b \sqrt{\rho(\varepsilon)} \quad [2]$$

via the strain dependence of the total (mobile and immobile) dislocation density ρ

$$\frac{d\rho}{d\varepsilon} = \frac{M}{b s(\varepsilon)} - \Omega\rho. \quad [3]$$

σ_0 is the friction stress of dislocation movement, α a constant close to one, G the shear modulus, b the magnitude of the Burgers vector, $s(\varepsilon)$ the mean free distance for dislocations, M the Taylor factor, and Ω is a constant that represents the rate of remobilization of the immobile dislocations.

As the theory was developed, different expressions were suggested for $s(\varepsilon)$.[19,21] However, we found that even another expression, namely

$$\frac{ds(\varepsilon)}{d\varepsilon} = -k_s s(\varepsilon)^2 \quad [4]$$

which, after integrations, yielded

$$s(\varepsilon) = \frac{s(0)}{1 + \varepsilon k_s s(0)} \quad [5]$$

was better suited to describe the tensile test curves of our braze-clad AA3003 alloy after braze simulation; the previously suggested expressions for $s(\varepsilon)$ were not adequate in our case. k_s is a constant. After insertion of Eqs. [2], [4], and [5] into Eq. [3], integration of Eq. [3] and insertion into Eq. [2], we arrived at the expression

$$\sigma(\varepsilon) = \sigma_0 + H\sqrt{1 + \beta\varepsilon - e^{-\Omega\cdot\varepsilon}}, \quad [6]$$

where σ_0, H, β, and Ω are fitting parameters.

The regression curves are in almost perfect agreement with the measured data, as shown in Figure 6(a). This might not come as a complete surprise, considering that four parameters have been fitted during the regression. Nevertheless, the standard errors of the regression parameters are very small which means that Eq. [6] describes the true stress–true strain curve very well. The regression parameters and their standard errors are given in Table III.

The dependences of the regression parameters upon temperature are well described by third-order polynomial functions whose curves have been plotted as dashed lines in Figure 6(b). For each regression parameter, an estimated value can now be calculated from the corresponding polynomial function for any temperature between 293 K and 573 K (20 °C and 300 °C). Therefore, Eq. [6] can be used to calculate interpolated true stress–true strain curves at any temperature between 293 K and 573 K (20 °C and 300 °C) where experimental data are not available.

Figure 6(c) shows the experimentally determined true stress–true strain curves again, this time together with the interpolated curves. The agreement between measured data and the curves calculated from the interpolation function is really good. Interpolated true stress–true strain curves at 423 K and 498 K (150 °C and 225 °C) have been added and demonstrate the usefulness of the interpolation procedure.

The procedure was successfully applied also to Alloy-A through Alloy-D of Table I. However, we did not succeed to fit the modified Bergström model to the true stress–true strain curves of Alloy-E at room temperature. The formation of Mg- and Si-clusters during natural aging[22] might have caused the material to deform in a different way, such that our version of the concept of a mean free distance for dislocations was not applicable in this particular case.

C. *Fatigue Test Results*

Fatigue test results for AA3003 are depicted in Figure 7. The fatigue strength, expressed in terms of stress amplitude for failure after a certain number of cycles, decreases strongly with increasing temperature.

Fatigue stress amplitudes for 10^5 and 10^6 cycles to failure are shown in Figures 8(a) and (b) for four heat exchanger tube alloys. All stress amplitudes have been normalized to the value at 373 K (100 °C) for the respective alloy in order to more clearly show the general trend. The absolute stress amplitudes for a certain number of cycles to failure of course differed between the different alloys.

Not enough fatigue data were available to include Alloy-D. Alloy-E exhibited significant Mg-Si precipitation hardening during the fatigue test at 453 K (180 °C) while over-aging occurred at 523 K (250 °C). This had a strong influence on the S–N curves and will be discussed further below.

The values shown in Figure 8 were calculated from fit lines, as shown for AA3003 in Figure 7. We had previously found for strain-controlled flexural fatigue testing of heat exchanger tube alloys that the fatigue strength did not decrease significantly with increasing temperature for temperatures below 473 K (200 °C).[23] However, the influence of temperature is stronger for stress-controlled fatigue tests than for strain-controlled fatigue tests. An increase in temperature increases the total strain amplitude for the case of stress-controlled testing because the material's resistance to plastic deformation decreases with increasing temperature. For strain-controlled testing, on the other hand, the temperature increase does not affect the total strain amplitude; only the fraction of plastic strain is increased due to the reduction in yield strength.

In the range from 10^5 to 10^6 cycles, most stress amplitude-fatigue lifetime (S–N) curves can be described rather well by a power law,

$$\ln(N) = a\ \ln(\Delta\sigma) + \ln(b) \quad [7]$$

where ln (N) is fitted to $\ln(\Delta\sigma)$ by linear regression, with a and b as fit parameters; this relation is often called the "Basquin law." The dashed lines in Figure 7 represent separate fits of Eq. [7] to the S–N curves at the different temperatures.

Figure 9 shows a strong scatter in the Basquin fit parameter a with temperature. This scatter is attributed

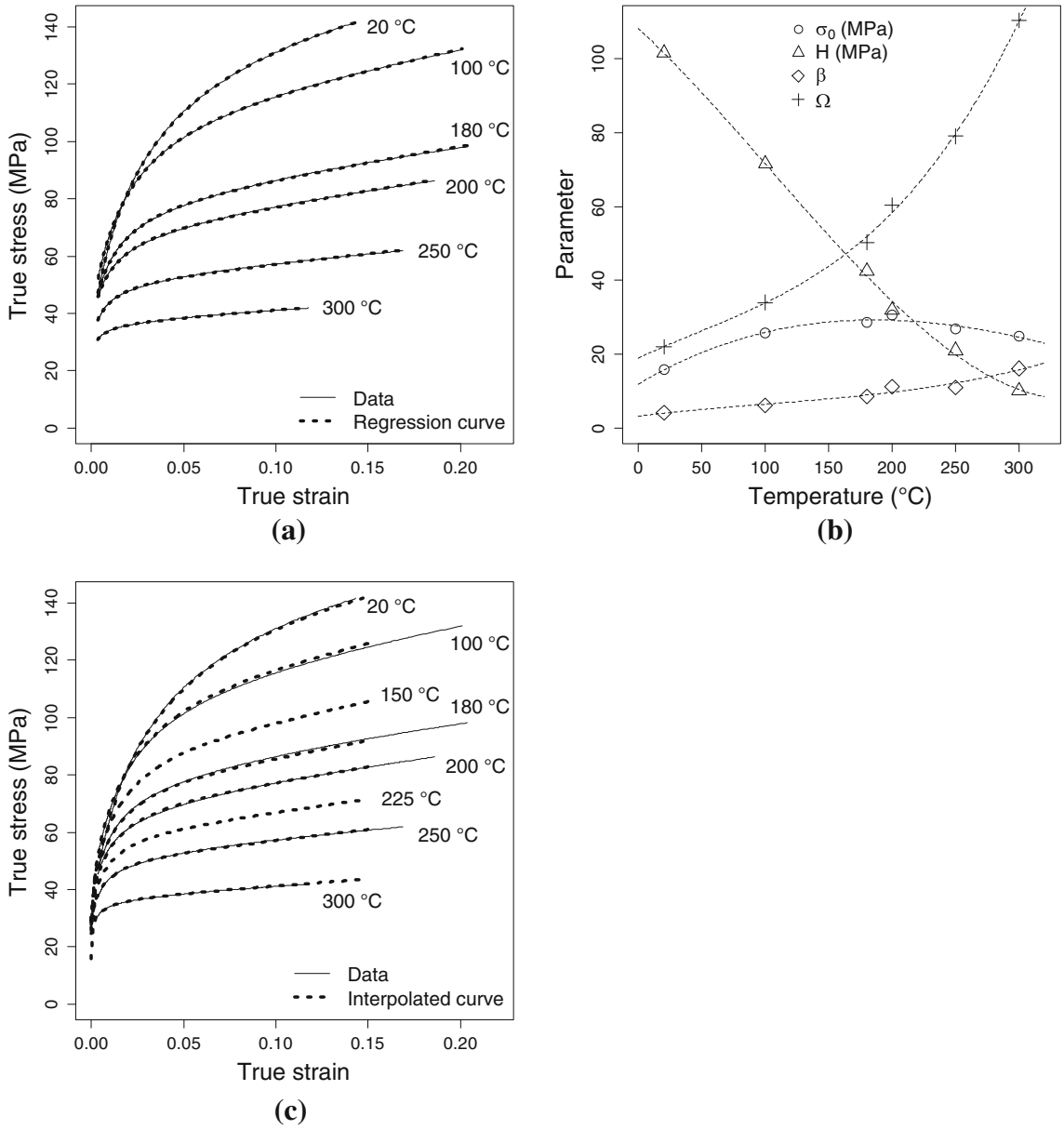

Fig. 6—True stress–true strain curves for AA3003 at different temperatures. (*a*) Experimental data and regression curves from data fitting by Eq. [6]. (*b*) Regression parameters *vs* testing temperature, dashed lines represent third-order polynomial functions. (*c*) Experimental data and curves calculated from Eq. [6], using parameter values from the third-order polynomial functions.

Table III. Regression Parameters and Their Standard Errors for Fitting of Eq. [6] to Averaged True Stress–True Strain Curves of AA3003 at Different Temperatures

Temperature [K (°C)]	σ_0 (MPa)	H (MPa)	β	Ω
293 (20)	15.74 ± 0.09	101.5 ± 0.5	4.0 ± 0.1	22.0 ± 0.2
373 (100)	25.69 ± 0.05	71.59 ± 0.06	6.09 ± 0.02	34.4 ± 0.1
453 (180)	28.60 ± 0.09	42.51 ± 0.08	8.44 ± 0.04	50.3 ± 0.3
473 (200)	30.5 ± 0.1	31.90 ± 0.09	11.22 ± 0.06	60.4 ± 0.5
523 (250)	26.7 ± 0.1	21.0 ± 0.1	10.96 ± 0.09	79 ± 1
573 (300)	24.77 ± 0.09	10.11 ± 0.08	16.0 ± 0.2	111 ± 2

to the scatter in lifetimes over the range where the power law is valid, and the small number of data points of any given alloy. From inspection of Figure 7, an increase in magnitude of the (negative) fit parameter a is expected. By averaging all of the data for the full range of alloys and temperatures, the expected monotonic decrease in

the parameter a with temperature is observed, but the Pearson coefficient for this correlation is only −0.35.

Due to the large scatter in the temperature dependence of the parameters of the Basquin law, we cannot suggest any procedure that is analogous to the procedure that we have applied to derive interpolated true stress–true strain curves from tensile test data.

Kohout[24] suggested that the fit parameter a was temperature-independent and proposed an extension of the Basquin law to include a power law-dependence of the stress amplitude on the testing temperature, $\Delta\sigma \propto T^c$, $c < 0$, where c is the so-called temperature sensitivity parameter. This extension of the Basquin law proved to be a good description of the low-temperature dependence of the fatigue strength of other materials, including an AA6101-T6 aluminum alloy.[24,25]

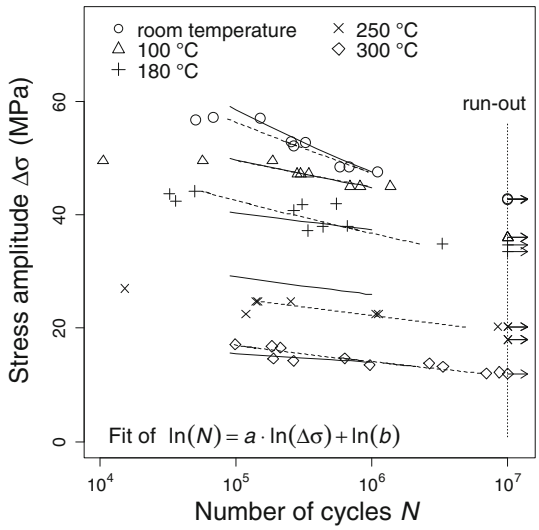

Fig. 7—Stress amplitude-fatigue life data of 0.40-mm-thick braze-simulated, braze-clad AA3003 heat exchanger tube alloy at different temperatures. Load ratio and test frequency were $R = 0.1$ and 30 Hz. Dashed lines correspond to separate fits of Eq. [7], solid lines to a common fit for several alloys where Eqs. [8] and [9] have been used to describe the temperature dependence.

However, Figure 10 with both axes in logarithmic scale demonstrates that the temperature dependence of our braze-simulated heat exchanger tube materials was different—the data points do not follow straight lines. According to Kohout,[24] a deviation from the $\Delta\sigma \propto T^c$ dependence at elevated temperatures indicates that the fatigue strength is reduced by creep processes, *i.e.*, that two damage mechanisms are active simultaneously. Following this interpretation, we would expect that the fatigue strength in our materials was reduced by creep processes already at temperatures between 373 K and 453 K (100 °C and 180 °C).

For secondary creep strain rate and creep rupture strength, formalisms that include both the stress and temperature dependences have been discussed for a long time. One such approach will be considered in Section III–D. However, we are not aware of any equation that is able to describe the stress and temperature dependence of combined high-cycle fatigue and creep loads.

For this reason, we resort to a simple pragmatic approach in order to predict S–N curves for temperatures where S–N fatigue data are not available. The temperature dependence of the normalized fatigue strengths at 10^5 and 10^6 cycles to failure can be

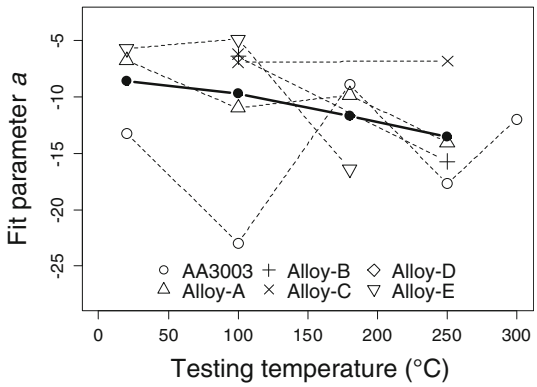

Fig. 9—Evolution of fit parameter a with temperature. Open symbols are parameters obtained for the different alloys, solid circles mark the mean values over all alloys.

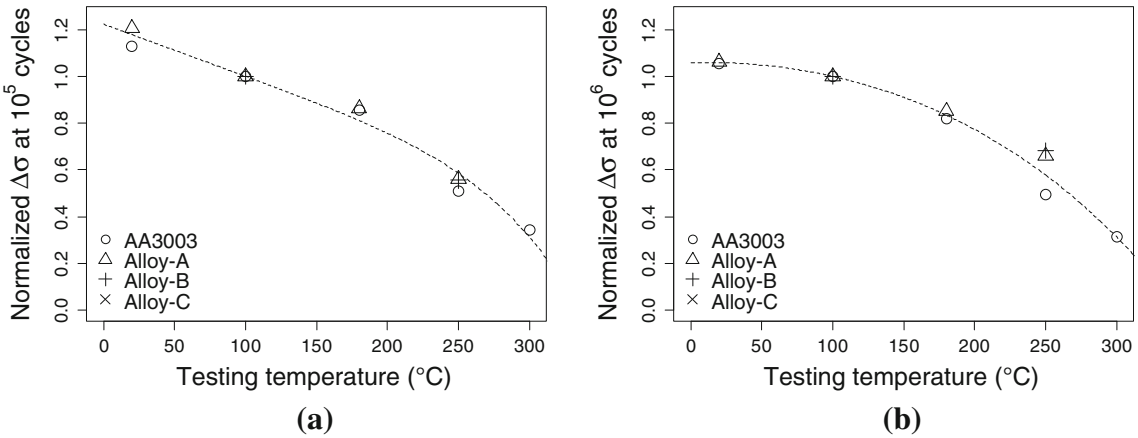

Fig. 8—Fatigue stress amplitude, normalized to the respective value at 373 K (100 °C), at (*a*) 10^5 cycles and (*b*) 10^6 cycles as a function of temperature. Only alloys without Mg-Si precipitation hardening and with data available at 373 K (100 °C) were included. The dashed lines represent Eqs. [8] and [9].

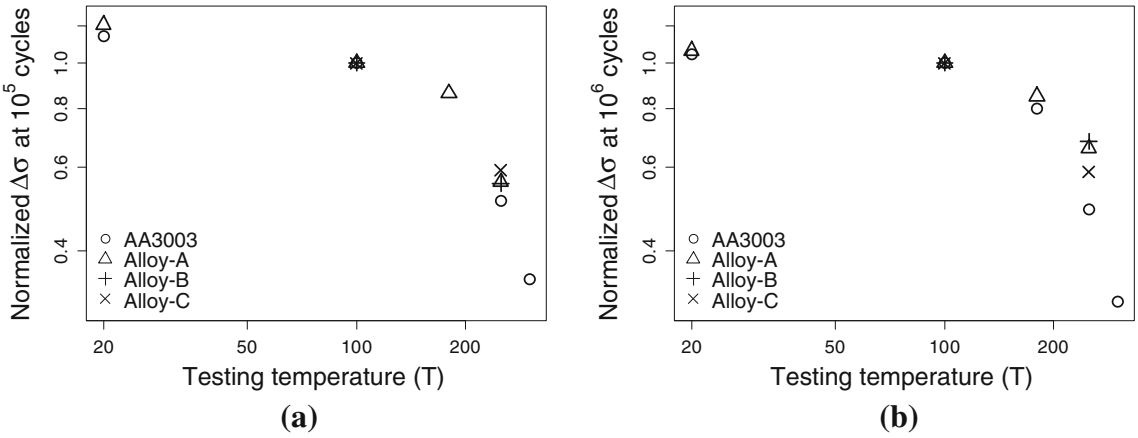

Fig. 10—Fatigue stress amplitude, normalized to the respective value at 373 K (100 °C), as a function of temperature, presented in double logarithmic scale for three heat exchanger tube alloys. (*a*) 10^5 cycles and (*b*) 10^6 cycles.

described rather well by simple polynomial expressions, as indicated by the dashed lines in Figure 8. The dashed lines in Figure 8(a) are given by

$$\left.\frac{\Delta\sigma}{\Delta\sigma_{T=100\,^\circ\mathrm{C}}}\right|_{N=10^5} = 1.23 - \frac{2.34\times10^{-3}}{^\circ\mathrm{C}}\,T - \frac{2.78\times10^{-16}}{(^\circ\mathrm{C})^6}\,T^6 \quad [8]$$

$$\left.\frac{\Delta\sigma}{\Delta\sigma_{T=100\,^\circ\mathrm{C}}}\right|_{N=10^6} = 1.05 + \frac{1.91\times10^{-4}}{^\circ\mathrm{C}}\,T - \frac{7.42\times10^{-6}}{(^\circ\mathrm{C})^2}\,T^2 - \frac{1.60\times10^{-11}}{(^\circ\mathrm{C})^4}\,T^4. \quad [9]$$

For the Basquin law, we can now calculate the coefficients a and b from Eqs. [8] and [9] for any temperature where these two equations are assumed to be valid. From Figure 7, the agreement between the S–N curves based on Eqs. [8] and [9] with the measured data can be assessed. The closeness of agreement is obviously directly related to the difference between fitted curve and data point of the respective alloy—here AA3003—in Figure 8. At 453 K (180 °C), the normalized fatigue strengths at both 10^5 and 10^6 cycles to failure are below the fitted curve; therefore, the estimated fatigue strength (solid line) is a bit too high at this temperature.

While Eqs. [8] and [9] can be used to predict S–N curves for any of the four alloys from Figure 8 at any temperature between 293 K and 573 K (20 °C and 300 °C), the agreement with the data points is clearly better for the separately fitted Basquin equations than for the combined fit.

We mentioned previously that the S–N curves of Alloy-E were strongly influenced by Mg-Si precipitation. Figure 11 shows fatigue curves for this material after several weeks of natural aging and after several weeks of natural aging plus a static heat treatment for the indicated time at the testing temperature, prior to the fatigue test.

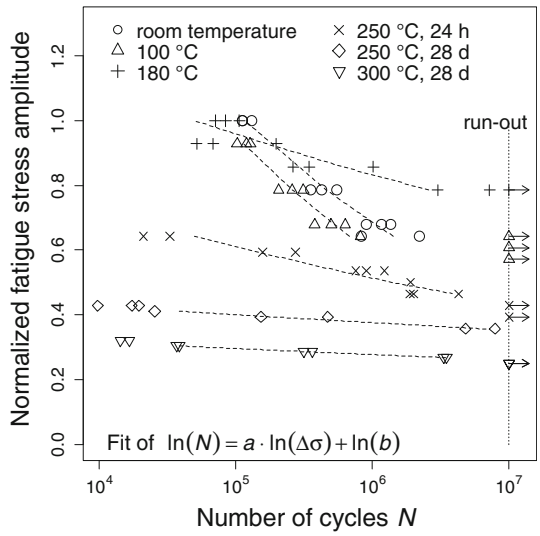

Fig. 11—Stress amplitude-fatigue life data for Alloy-E at different temperatures, normalized to the maximum stress amplitude. Dashed lines correspond to separate fits of Eq. [7] for each temperature. The specimens tested at 523 K and 573 K (250 °C and 300 °C) were kept for the indicated time at the testing temperature prior to the test.

Naturally aged material possesses higher fatigue strength at 453 K (180 °C) than at the lower testing temperatures for high numbers of cycles. The reason for this behavior is that the material is further strengthened by artificial aging during the fatigue test at 453 K (180 °C). The combination of temperature and deformation in AA6XXX series alloys leads to enhanced precipitation kinetics and changed precipitation sequence as compared to static heat treatment.[26–28]

The fatigue strength at 523 K (250 °C) of the material that had been heat-treated for 28 days at testing temperature is significantly smaller than the fatigue strength of the material that had been heat-treated for only 24 hours; a heat treatment of 28 days at 523 K (250 °C) causes strong over-aging of the Mg-Si precipitates and a corresponding loss of the strengthening effect from these precipitates.

Although Table II indicates a strong correlation between fatigue strength and tensile strength, we are convinced that fatigue strength should not generally be deduced from tensile properties. We can best exemplify our point when we compare tensile properties and fatigue strength of Alloy-A and Alloy-E at room temperature. This comparison is shown in Table IV. Alloy-E has 31 pct higher tensile strength and 12 pct higher elongation than Alloy-A, but Alloy-A has higher fatigue strength, especially at 10^6 cycles to failure.

During the fatigue test, slip lines developed at the milled edges of the specimen sections of reduced width as shown in Figure 12(a). For fatigue test temperatures not exceeding 373 K (100 °C), almost all fatigue cracks nucleated at these edges. The crack shown in Figure 12(b) was observed on a specimen that had already fractured at another location. Observation of such cracks was extremely rare.

One special question with respect to fatigue loading is how much of the total fatigue lifetime is required to nucleate a crack. During the simulated brazing, the materials became soft. In addition, tube alloys are thin and elevated-temperature fatigue tests were carried out inside closed furnaces. Therefore, we could not apply common methods for crack detection and observation.

We based our effort to estimate the time for crack nucleation in Alloy-A at 373 K (100 °C) on the following assumptions: (1) Fatigue lifetimes N follow a lognormal distribution. This means that $\ln N$ follows a normal distribution with mean $\overline{\ln N}$ and standard deviation $S_{\ln N}$. (2) Crack initiation times N_i also follow a lognormal distribution, with $S_{\ln N_i} = S_{\ln N}$ and $\overline{\ln N_i} = \overline{\ln N} - C$, where C is a constant that describes the shift between the two distributions on the $\ln N$ axis. (3) The ratio N_g/N of the crack growth time $N_g = N - N_i$ to the total fatigue lifetime N is the same for all values of N; this requires that the specimen with the shortest N_i has the shortest N_g, the specimen with the second shortest N_i has the second shortest N_g and so forth.

The above considerations are schematically shown in Figure 13. The arrows represent the times for fatigue crack growth and are all of length C in the logarithmic scale of the figure. Assumption (3) was made for mathematical convenience. The general trend is that N_g/N is higher in the low-cycle fatigue regime than in the high-cycle fatigue regime[29]; in the experiment described here, the fatigue stress amplitude was the same for all specimens tested at 373 K (100 °C).

In a first fatigue test series, $n_{1st} = 12$ specimens were cycled to fracture at the stress amplitude of 57 MPa. From this series of specimens, the number of cycles $N_{2nd} = 470{,}000$ was determined where three specimens had failed. In the second test series, $n_{2nd} = 12$ specimens were cycled at the same load as during the first series, but testing was interrupted at N_{2nd}. We chose the value of N_{2nd} according to two criteria: (1) Most specimens should be survivors at N_{2nd} in order to have many non-fractured specimens left that might have developed a crack. (2) Shortly beyond $\ln N_{2nd}$, the cumulative failure probability curve should have its region of maximum slope in order to increase the probability of observing fatigue cracks.

If the distribution functions for crack initiation and for failure had had the shapes as depicted in Figure 13, specimens 4 through 7 would have developed a fatigue

Table IV. Comparison of Tensile Properties and Fatigue Strength for Alloy-A and Alloy-E

Alloy	$R_{p0.2}$	R_m	A_g	A_{50mm}	Fatigue 10^5 Cycles	Fatigue 10^6 Cycles
Alloy-A	1	1	1	1	1	1
Alloy-E	1.67	1.31	1.13	1.12	0.93	0.86

All quantities have been normalized with respect to the values measured for Alloy-A. Fatigue strength at the indicated number of cycles to failure has been expressed in terms of stress amplitude. Properties of Alloy-E are given for 14 days of natural aging subsequent to the simulated brazing.

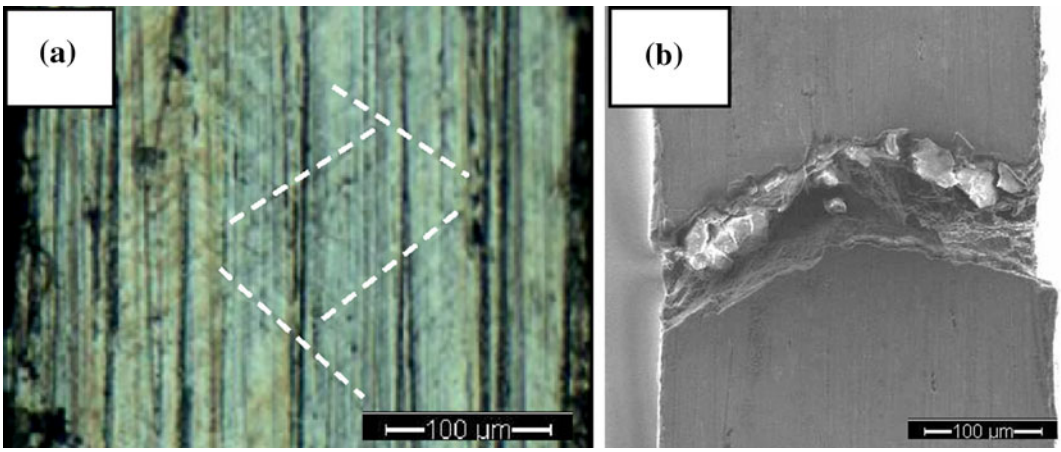

Fig. 12—Edges of fatigue test specimens made from Alloy-A, loaded at 373 K (100 °C), showing (*a*) slip lines, (*b*) a small crack. Four slip lines in (a) are marked by dashed lines.

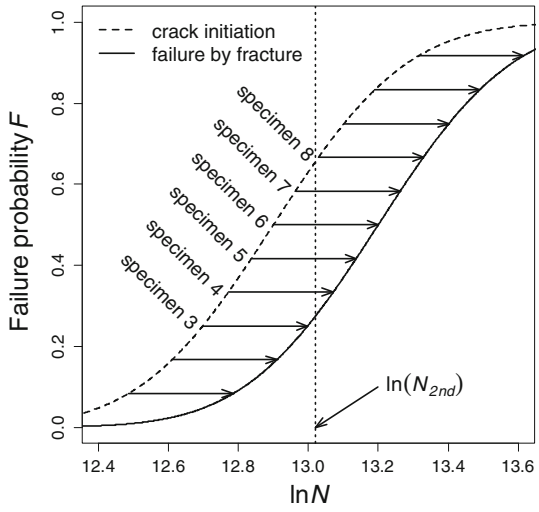

Fig. 13—Schematic drawing to explain the assumptions made for estimation of the times required for fatigue crack initiation and fatigue crack growth.

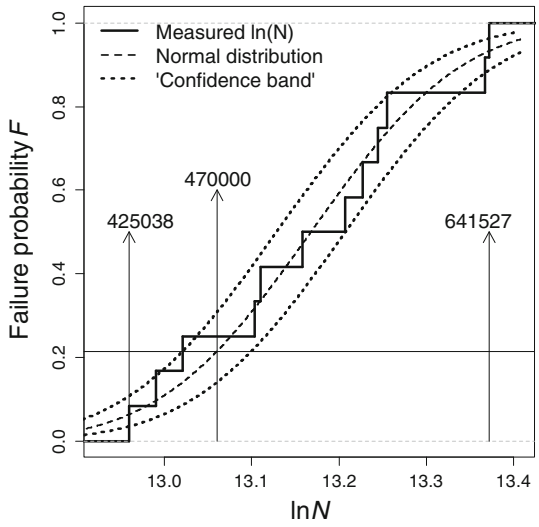

Fig. 14—Cumulative failure probability *vs* logarithm of number of cycles ln N to failure for 12 specimens prepared from Alloy-A. The dashed line represents the Gaussian distribution function for ln N, numbers inside the figure indicate numbers of cycles. Further details are explained in the text.

crack at N_{2nd}. From the second test series, the fatigue cracks of specimens 4 to 7 would have been observed by metallographic investigations of the milled specimen edges and we would have obtained an estimate for C.

The actual results were the following. One specimen of the second series failed before N_{2nd} was reached while the others were run-outs at this number of cycles. We investigated all run-out specimens in the SEM, but we did not find any crack on any of these.

While these results already indicated that the time for fatigue crack initiation was very large as compared to the time for crack growth, we also estimated an upper bound for the crack growth time. The upper bound corresponds roughly to an error of one standard deviation and the estimation procedure is explained with the help of Figure 14.

(1) The error in determining the Gaussian distribution function F_G (represented by the dashed line) from the measured data of the first test series was set equal to a shift of the dashed line by the standard deviation of the mean value of the logarithmic lifetime, $S_{\overline{\ln N}}$. The corresponding "confidence band" is shown by the two dotted lines. (2) The experimental error in deciding whether a crack had formed or was not set equal to one false decision on n_{2nd} samples, corresponding to an error of $1/n_{2nd}$. (3) The upper bound for N_g was then calculated from the probability $F_G(\ln N_{2nd}) + 1/n_{2nd}$ and from the dotted line that corresponds to a mean logarithmic lifetime to fracture of $\overline{\ln N} + S_{\overline{\ln N}}$. The upper bound for N_g is represented by the horizontal arrow and corresponds to 36,419 cycles.

We therefore expect the time for fatigue crack growth to be a fraction of between 0 and 7 pct of the total fatigue lifetime.

An analogous investigation carried out at 523 K (250 °C) yielded a similar result; we did not find any crack in any of the surviving specimens of the second fatigue test series.

Recently, the time to crack initiation was measured during fatigue testing of flat specimens at room temperature by Buteri *et al.*[6] Specimens were braze-simulated in such a way that well pronounced clad solidification droplets accumulated on the specimen surfaces. After 97 pct of the fatigue lifetime, no crack or strain heterogeneity was observed, where a crack of 1 mm length was defined as failure of the specimen. These authors thus arrived at the same conclusion as we did, namely, that the time for crack initiation dominated the total fatigue lifetime.

Since all deformation hardening was removed during the simulated brazing, the materials have a strong strain hardening potential at the beginning of the fatigue test, especially at low testing temperatures; this also becomes obvious from Figure 4(c).

We monitored the position of the hydraulic cylinder that was the actuator during the fatigue tests. For these experiments, the test frequency of the first 50 cycles was reduced to 0.1 Hz in order to minimize the ramp up effects that occurred at regular test frequencies. After 50 cycles, the frequency was ramped up from 0.1 to 27 Hz. During standard testing, the fatigue tests started at full frequency whereas the stress amplitude was ramped up over the first few hundred cycles. The testing device's compliance was measured with a massive steel sample and all data presented here were corrected for the elastic deformation of the testing device.

In the following, we will discuss two tests: One test at room temperature where the specimen failed after 12,844 cycles and one test at 453 K (180 °C) where the specimen failed after 88,168 cycles. The results are displayed in Figure 15.

At room temperature, the specimen elongated by almost 3 mm during the first cycle. During the subsequent cycles, the cylinder displacement per cycle decreased strongly and reached a value close to zero already during the fourth cycle. After the maximum force had been reached during the fourth cycle, no further elongation of the specimen occurred.

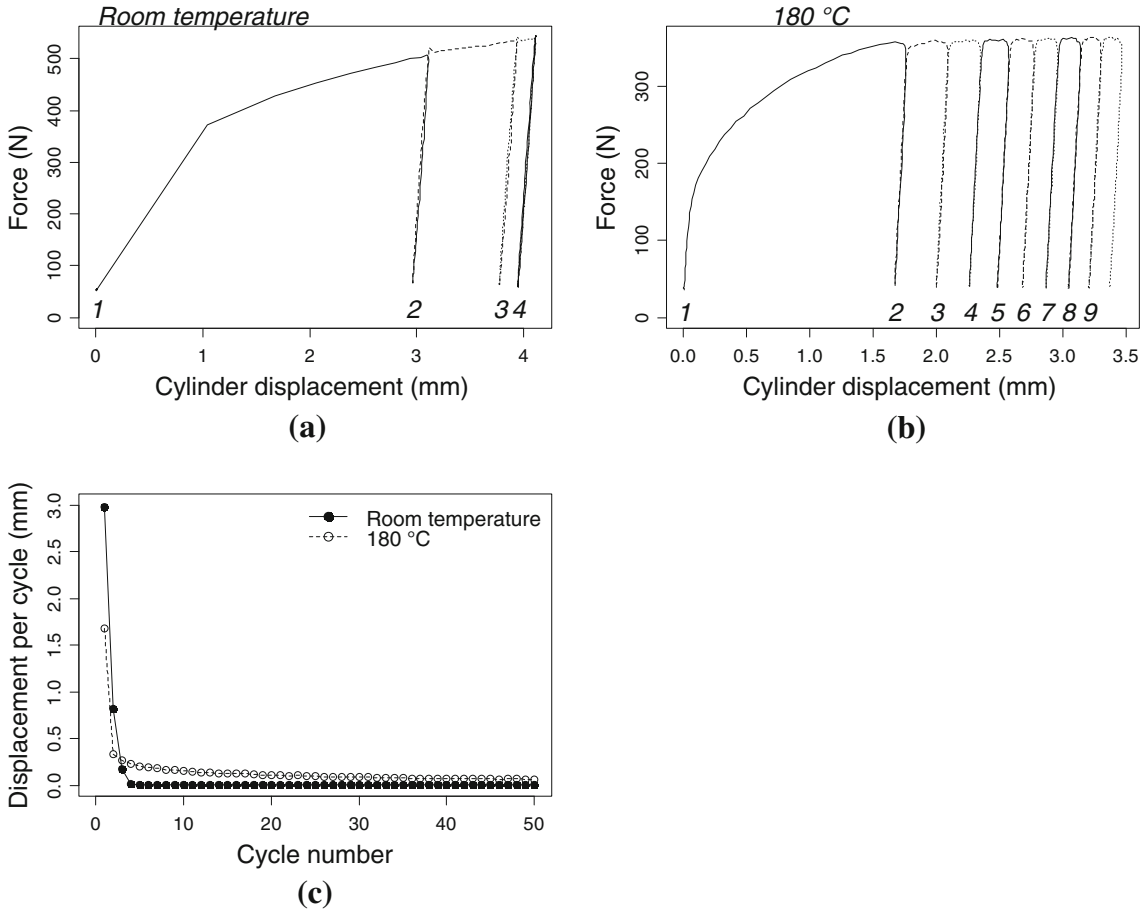

Fig. 15—Force–displacement curves for the first fatigue cycles, carried out at the reduced frequency of 0.1 Hz on Alloy-A, (*a*) at room temperature, (*b*) at 453 K (180 °C). Displacement was measured from the position of the hydraulic cylinder of the fatigue test device. Displacements per cycle are compared for both testing temperatures in (*c*).

At 453 K (180 °C), the displacement of the first cycle was also stronger than during the subsequent cycles, but the specimen continued to elongate during each of the 50 first cycles although the maximum force had already been reached. This indicates that creep contributes to the specimen elongation at this temperature. Therefore, the fatigue strength will depend on test frequency at temperatures of 453 K (180 °C) and above. Cylinder displacement per cycle is expected to increase with decreasing test frequency for two reasons: The time at tensile load increases and the strain rate decreases when the frequency decreases.

Juijerm *et al.*[25,30] concluded that cyclic creep started to play a dominant role in fatigue testing of both hot-rolled AA5083 and extruded AA6110-T6 for temperatures above 473 K (200 °C). These results are in good agreement with the fact that we observed signs of creep during fatigue testing at 453 K (180 °C).

D. *Creep Rupture Test Results*

The results from creep rupture tests of AA3003 are shown in Figure 16. Creep rupture strengths were in the

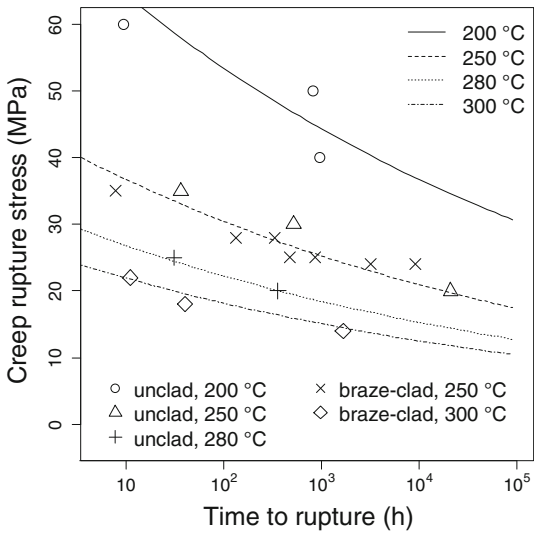

Fig. 16—Creep–rupture curves for braze-simulated AA3003. Measured data are given by symbols, curves were calculated from Eq. [16] with the regression parameters given in Table V.

same range as the stress amplitudes of the fatigue test and also decreased significantly with increasing temperature.

It has often been assumed that the time to rupture at a given stress level will vary in such a way that the Larson–Miller parameter $T(C + \log t_R)$, with C a constant and t_R the time to rupture or creep lifetime, remains unchanged.[31] This approach did not describe our results well. We therefore decided to describe our creep data by the Mukherjee–Bird–Dorn (MBD) equation[32]

$$\frac{\dot{\varepsilon} k T}{D G b} = A \times \left(\frac{\sigma}{G}\right)^n, \qquad [10]$$

where $\dot{\varepsilon}$ is the steady-state creep strain rate, k the Boltzmann constant, D the diffusivity, G the shear modulus, b the Burgers vector, and A is a constant. For pure aluminum, a stress exponent n of 4.4 was reported.[32] The diffusivity is given by

$$D = D_0 e^{-Q/kT}, \qquad [11]$$

where Q is often the activation energy for self-diffusion and D_0 the diffusivity constant.

In alloys, the influence of the microstructure is more complex, and it is possible that other activation energies are found than that for self-diffusion. In the treatment of work hardening and flow at elevated temperatures by Nes,[33] the activation energy represented the interaction between mobile dislocations and solute atoms. The temperature dependence of the shear modulus G is not negligible and must be considered.

The MBD equation is valid for the creep regime that is dominated by diffusional creep. At stress levels higher than around $5 \times 10^{-4} G$ to $10^{-3} G$, the MBD equation may break down and the creep strain rates may increase exponentially.[34] For AA3XXX series aluminum with $G \approx 26$ GPa, this corresponds to a stress range of 13 to 26 MPa.

Since the secondary creep strain rate represents the slowest creep strain rate, secondary creep should take up the largest part of the time to rupture. The time to rupture should then show similar temperature dependence as the secondary creep strain rate and thus similar activation energy. It is less probable that the primary and tertiary creep rates should show similar stress dependence as the secondary creep. The creep lifetime may therefore be related to the steady-state creep strain rate by the Monkman–Grant relation,

$$\dot{\varepsilon} t_R^{\eta} = C_{MG}, \qquad [12]$$

where $\eta \approx 1$ and C_{MG} are constants.[35]

We combined Eqs. [10] and [11] to obtain

$$\ln\left(\frac{\dot{\varepsilon} T}{G}\right) = n \ln\left(\frac{\sigma}{G}\right) - \frac{Q}{kT} + c_1, \qquad [13]$$

where c_1 is a constant. Use of Eq. [12] yielded

$$\ln\left(\frac{t_R G}{T}\right) = -n \ln\left(\frac{\sigma}{G}\right) + \frac{Q}{kT} + c_2, \qquad [14]$$

where c_2 is a constant. Since values for the shear modulus at different temperatures were not available for the alloys under investigation, we worked instead with the temperature variation of the elastic modulus E as determined by tensile tests. A fit of the data for AA3003-O, given in Reference 36, by a polynomial expression of fifth order gave:

$$\frac{E}{\text{GPa}} = \frac{3.48 \times 10^{-12}\ T^5}{(^\circ\text{C})^5} - \frac{5.70 \times 10^{-10}\ T^4}{(^\circ\text{C})^4} - \frac{6.58 \times 10^{-7}\ T^3}{(^\circ\text{C})^3} - \frac{3.12 \times 10^{-5}\ T^2}{(^\circ\text{C})^2} - \frac{2.98 \times 10^{-2}\ T}{^\circ\text{C}} + 69.29. \qquad [15]$$

This temperature dependence of the elastic modulus significantly deviates from that given in Reference 37 for pure aluminum. In the following, we will use Eq. [15] in combination with the following modified version of Eq. [14],

$$\ln\left(\frac{t_R E}{T}\right) = -n \ln\left(\frac{\sigma}{E}\right) + \frac{Q}{kT} + c_3 \qquad [16]$$

where c_3 is a constant.

Equation [16] was derived for creep tests performed under constant stress whereas our creep–rupture curves were obtained under constant force. On the other hand, creep strain to rupture varies between different specimens, and the Monkman–Grant relation is not strictly valid anyway. Especially the stress exponent n does therefore no longer have the same meaning as the n of Eq. [10].

From fitting of Eq. [16] to the data shown in Figure 16, we obtained the regression parameters given in Table V. The value obtained for Q agrees within the error margin with the activation energies in the range of 2.16 to 2.25 eV for bulk diffusion of manganese in aluminum, reported in the Reference 38.

The curves in Figure 16 were calculated from Eq. [16] with the parameters of Table V. The agreement between the measured data and the calculated curves is very good and implies that interpolated creep rupture curves of braze-simulated AA3003 can be calculated with satisfactory accuracy for testing temperatures between 473 K and 573 K (200 °C and 300 °C).

The validity of Eq. [16] for our data is confirmed in Figure 17 where the left-hand-side of Eq. [16] is shown to be a linear function of $\ln(\sigma/E)$. Note that we have

Table V. Regression Parameters and Standard Errors from Fitting of Eq. [16] to Creep–Rupture Data of Braze-Simulated AA3003, Both Braze-Clad and Unclad

Q (eV)	n	c_3
2.44 ± 0.28	12.3 ± 1.3	−114 ± 15

used data with creep rupture strength of up to 70 MPa, which is significantly higher than recommended by Reference 34.

Reference 36 probably constitutes the most comprehensive source for mechanical properties of aluminum alloys at various temperatures. This reference gives consolidated creep data for AA3003-O, *i.e.*, for AA3003 after soft-annealing. Fitting Eq. [16] to data for creep rupture strengths below 70 MPa yielded the following regression parameters: $Q = 1.43 \pm 0.03$, $n = 11.1 \pm 0.2$, $c_3 = -87 \pm 2$. The standard errors of the regression parameters are artificially low here because the data had already been consolidated by the author of Reference 36. The value of Q is now below the activation energy for bulk diffusion of manganese in aluminum and very close to the activation energy for self-diffusion in aluminum, given as 1.47 eV in Reference 32. Reference 37 states that most of the activation energies for self-diffusion in aluminum given in the literature are in the range 1.2 to 1.3 eV.

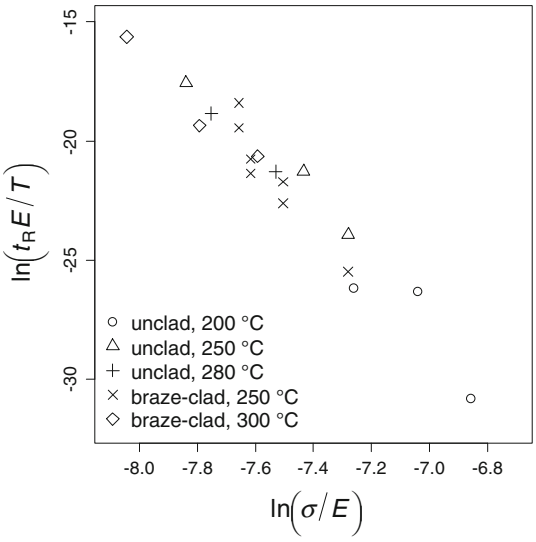

Fig. 17—Plot of the left-hand-side of Eq. [16] against $\ln(\sigma/E)$, with the purpose to confirm the validity of Eq. [16] for the creep–rupture data of braze-simulated AA3003, both braze-clad and unclad.

Since our material was heated to 873 K (600 °C) during the simulated brazing and then quickly cooled down in forced air to room temperature, significantly more manganese atoms are expected to be in solid solution than after soft-annealing of the AA3003-O material. This could explain the difference in activation energies between our data and the data from Reference 36.

The above-presented approach of how to describe the stress and temperature dependence of AA3003 by a model with three fitting parameters was applicable to all six alloys given in Table I.

The evolution of normalized creep rupture strength with temperature is depicted in Figure 18. It is noteworthy that the curvature is positive—in agreement with Eq. [16]—whereas the curvature of the fatigue strength evolution with temperature was negative, compare with Figure 8. This means that the rate at which the creep rupture strength decreases with increasing temperature becomes smaller at higher temperatures while the opposite is true for fatigue strength.

Figure 18 also shows that the normalized data from different alloys all follow very similar temperature dependences. The variations in the temperature dependences of the tensile and fatigue strengths are much larger as can be seen from Figures 4 and 8.

Alloy-E had not been included into Figure 8 due to the aging and over-aging in the Mg-Si system, which markedly changed the mechanical properties during the fatigue test as shown in Figure 11. Nevertheless, the normalized creep rupture strength of Alloy-E exhibited the same temperature dependence as the creep rupture strengths of the other alloys. Since contributions of

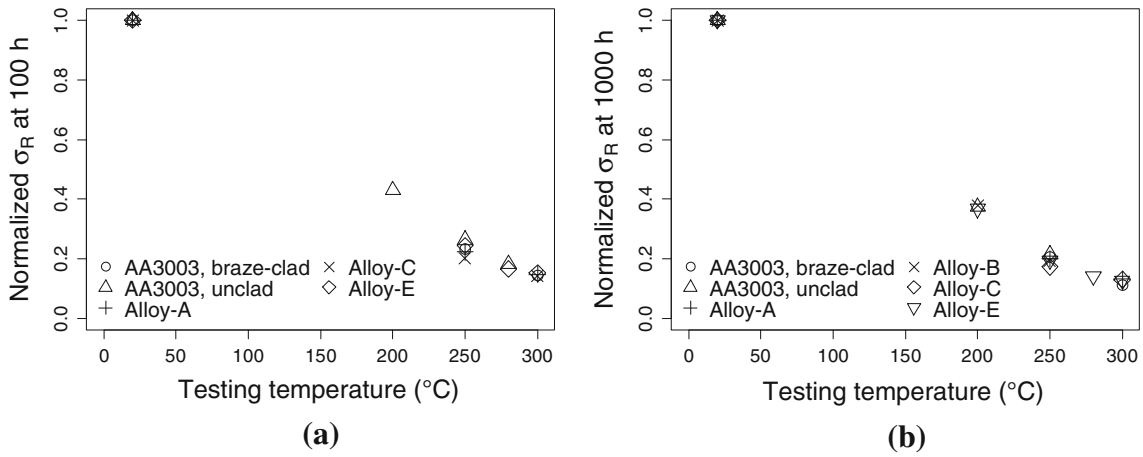

Fig. 18—Creep rupture strength, normalized to the respective tensile strength at 293 K (20 °C), as a function of temperature at (*a*) 100 h and (*b*) 1000 h to failure.

Mg-Si precipitates to mechanical strength are strongly reduced after only a few hours at 523 K (250 °C), these particles are not expected to significantly contribute to creep resistance.

On the other hand, the different alloys shown in Table I possess significant variations in their populations of intermetallic particles because of their different compositions. Such particles, based on the alloying elements silicon, iron, copper, manganese, magnesium, zirconium, and titanium, are more stable at elevated temperatures than Mg-Si precipitates are. Also the solid solution levels of silicon, copper, manganese, magnesium, and titanium are expected to vary significantly between the six different alloys.

Indications exist that manganese atoms in solid solution lead to a stronger increase of creep strength than manganese atoms in dispersoids or particles.[8] This is in agreement with the fact that the strengthening effect of manganese-containing dispersoids strongly diminishes as the strain increases.[39] If we then hypothesize that creep strength is dominated by one strengthening mechanism in the alloys of this investigation, namely solid solution strengthening, it is plausible that the temperature dependency of normalized creep strength is very similar for the different alloys.

E. *Relation Between Fatigue and Creep at High Temperatures*

It has long been known that cyclic loads at elevated temperatures activate damage mechanisms that have aspects of both creep and fatigue. Depending on the starting point, such mechanisms can be considered as "time-dependent fatigue"[29] or as "fatigue-perturbed creep"[40] or "cyclic creep."[41,42] For aluminum or aluminum alloys, it was reported in several cases that load cycling between a high and a low tensile stress gives shorter lifetimes than static loading at the high stress.[40,41] It was also shown, though, that both acceleration and retardation of strain rates may occur in cyclic creep of aluminum, depending on stress, stress amplitude, and testing frequency.[42–44] Testing frequencies in these cyclic creep investigations did not exceed 1 Hz.[40–44]

In Section III–C, two indications were given that creep mechanisms reduced the fatigue strength at elevated temperatures: The temperature dependence of the fatigue strength did not follow the extended Basquin equation suggested by Kohout,[24] and the plastic strain during low-frequency fatigue loading of Alloy-A at 453 K (180 °C) increased from cycle to cycle.

From the data collected during our study, we can also see that the influence of mean stress as compared to the influence of stress amplitude on the specimen lifetime increases with increasing temperature.

In Figure 19, we have connected by dashed lines the data points that correspond to same specimen lifetimes at the respective temperatures, room temperature and 573 K (300 °C). From the slope of the line that connects

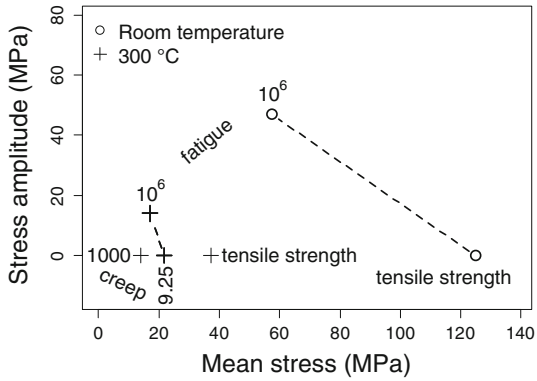

Fig. 19—Influence of stress amplitude and mean stress on specimen lifetimes at two different temperatures, for different types of mechanical tests. Numbers for fatigue tests indicate cycles to failure and numbers for creep tests hours to rupture. 106 cycles of fatigue testing correspond to 9.25 h test duration. Both axes of the figure have the same scale.

the data points at 573 K (300 °C), *i.e.*, the fatigue lifetime for 10^6 cycles to fracture at 30 Hz testing frequency and the creep rupture time of 9.25 hours, it can be seen that the influence of mean stress is stronger than the influence of stress amplitude on the specimen lifetime.

At room temperature, the situation is the opposite; the slope of the dashed line connecting the data points is less than one in magnitude, which means that stress amplitude has a stronger influence on specimen lifetime than mean stress. Since creep is negligible at room temperature, the constant stress that leads to specimen failure after 9.25 hours coincides with the tensile strength.

At 573 K (300 °C), the lifetime depends on the time at stress as is obvious from the creep test results. This is also true for the case of nonzero stress amplitudes and means that a reduction in fatigue testing frequency would lead to a reduction in number of cycles to failure.

It should be noted that data points from fatigue tests with a stress ratio $0.1 < R < 1$, other than $R = 0.1$ used in our fatigue tests, could deviate from the dashed lines in Figure 19[45]; these lines are only meant to connect the two data points at each temperature and to illustrate the general trend.

The dominating creep-type damage contribution during fatigue testing at high temperatures also becomes obvious from the fracture surfaces. Figure 20 shows the fracture surfaces of AA3003 specimens after fatigue and creep testing at 573 K (300 °C). Both fracture surfaces are characterized by very strong reductions in area and large cavities.

However, we should not expect that creep and fatigue loads at high temperatures generate exactly the same type of fracture and damage: The microstructure never reaches a stationary state during the fatigue tests where the applied stress varies sinusoidically with the testing frequency of 27 to 30 Hz.

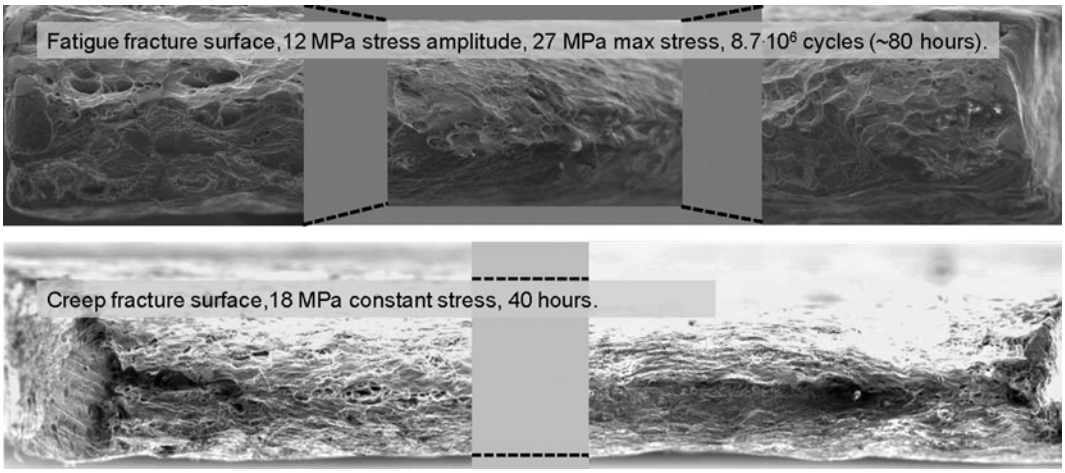

Fig. 20—Fracture surfaces of AA3003 specimens from fatigue and creep tests at 573 K (300 °C). Original material thickness is 0.40 mm.

IV. CONCLUSIONS

We have investigated tensile test, fatigue, and creep properties of five non-heat-treatable and one heat-treatable AA3XXX-series heat exchanger tube alloys for temperatures ranging from room temperature to 573 K (300 °C). All the materials were subjected to simulated brazing prior to measurement of mechanical properties.

Strong correlations were observed between tensile strength and fatigue strength after 10^5 cycles and creep strength after 100 and 1000 hours to failure, as well as between fatigue strength for failure after 10^5 and 10^6 cycles and creep strength after 100 and 1000 hours to failure. Nevertheless, ranking of alloys according to for example fatigue strength cannot be safely assumed to be the same as ranking according to for example tensile strength.

The main focus of this article has been on the dependences of the mechanical properties on temperature. We presented the temperature dependences of the mechanical properties of braze-clad AA3003, followed by the normalized temperature dependences of the mechanical properties of the other alloys.

Tensile deformation is characterized by low yield strength and high strain hardening at the lower temperatures and only mildly decreased yield strength but very small strain hardening at the higher temperatures of the investigated temperature range. The elongation of the material at the lower temperatures is caused by strain hardening whereas elongation at the higher temperatures is due to strain rate hardening; the uniform elongation has a maximum at around 423 K (150 °C).

Relative reductions in fatigue strength with increasing temperature were similar among the non-heat-treatable alloys. Alloy-E, on the other hand, exhibited pronounced strengthening by Mg-Si precipitation during the fatigue test at 453 K (180 °C) and significantly reduced fatigue strength after long-time over-aging at 523 K (250 °C).

We suggest that nucleation of a fatigue crack dominates the total fatigue lifetime for the fatigue tests of this investigation. This could be inferred from interrupted fatigue tests of Alloy-A at 373 K and 523 K (100 °C and 250 °C).

We found strong indications that creep reduces the fatigue strength already at testing temperatures between 373 K and 453 K (100 °C and 180 °C). At temperatures above 473 K (200 °C), we believe that creep mechanisms dominate the lifetimes during fatigue tests. Since the frequencies of service loads are much lower than the frequencies of fatigue tests, the relative importance of creep damage should be even higher in service than during our laboratory fatigue testing.

All six alloys closely follow the same relative change of creep rupture strength with increasing temperature. This indicates that the creep strength is sensitive to fewer microstructural details than tensile strength and fatigue strength are. The curvature of the strength-temperature relation is positive for creep strength, while it is negative for yield strength, tensile strength, and fatigue strength.

For tensile test, fatigue, and creep properties of our alloys, we found possibilities to interpolate to temperatures where data has not been measured.

To describe the true stress–true strain curves of the non-heat-treatable alloys, we developed a variant of the Bergström model with a new expression for the mean free distance of dislocation motion. Since the model parameters exhibit smooth temperature dependences, we can calculate interpolated true stress–true strain curves. Only the room temperature tensile curve of naturally aged Alloy-E did not follow the model.

Description of the temperature dependence of the fatigue strength was difficult because the fatigue lifetime was reduced by creep mechanisms at elevated temperatures. Since we were not aware of any suitable equation to describe the combined damage by high-cycle fatigue and creep processes in our alloys, we simply described the average evolution of fatigue strength with temperature by suitable polynomial expressions in combination with the Basquin equation. The case of Alloy-E was too complex for this approach because Mg-Si precipitates formed and over-aged during the fatigue tests and changed the alloy's fatigue resistance.

The stress and temperature dependence of the creep rupture strength can be represented by a combination of the MBD and the Monkman–Grant equations. Creep rupture strengths for all testing temperatures of one alloy are appropriately described by this model, which has three fitting parameters. The model was applicable to all six alloys of the present investigation.

ACKNOWLEDGMENTS

Financial support by the Sapa Heat Transfer R&D program on heat exchanger tube alloys is gratefully acknowledged. We are strongly indebted to our colleagues at Sapa Heat Transfer and Sapa Technology for inspiration, co-operation, and laboratory work. We would especially like to acknowledge Conny Widlund, Hans Carlsson, Ove Karlsson, Berit Bruun, Jozefa Zajac, Anders Oskarsson, Stefan Wass, and Lisa Åbom. We would also like to thank Per Sandahl and Gunnar Burman at Exova, Rui Wu at Swerea KIMAB, Lennart Johansson at Siemens Turbomachinery, and Gerd Neuse at Clausthal University for fatigue and creep measurements.

OPEN ACCESS

REFERENCES

1. J. Hirsch, ed.: *Virtual Fabrication of Aluminum Products*, WILEY-VCH, Weinheim, 2006, pp. 19–26.
2. ASM: Vol. 19, *Fatigue and Fracture*, ASM International, Materials Park, OH, U.S.A., 1996.
3. S. Meijers, A. Wittebrood, S. Desikan, and K. Vieregge: *AFC Holcroft Brazing Seminar*, 2005.
4. Low-Temperature-Joining-Committee: *Welding International*, vol. 22, 2008, pp. 669–75.
5. S. Kahl, J. Zajac, and H.-E. Ekström: *13th International Conference on Aluminum Alloys*, 2012.
6. A. Buteri, J.-Y. Buffière, D. Fabrègue, E. Perrin, J. Rethoré, and P. Havet: *12th International Conference on Aluminium Alloys*, 2010, pp. 338–44.
7. X.X. Yao, R. Sandström, and T. Stenqvist: *Mater. Sci. Eng. A*, 1999, vol. 267, pp. 1–6.
8. H. Hatta, S. Matsuda, and H. Yoshida: *Sumitomo Light Met. Tech. Rep.*, 2008, vol. 49, pp. 24–29.
9. H.H. Kim and S.B. Lee: *J. Mech. Sci. Technol.*, 2012, vol. 26, pp. 2111–15.
10. R-Development-Core-Team: *R: A Language and Environment for Statistical Computing*, R Foundation for Statistical Computing, Vienna, Austria, 2009.
11. K. Velten: *Mathematical Modeling and Simulation*, Wiley-VCH Verlag, Weinheim, 2009.
12. G.E. Dieter: *Mechanical Metallurgy*, McGraw-Hill Book Company, Singapore, 1988.
13. L. Blaz and E. Evangelista: *Mater. Sci. Eng. A*, 1996, vol. 207, pp. 195–201.
14. S.L. Semiatin, N. Frey, N.D. Walker, and J.J. Jonas: *Acta Metall.*, 1986, vol. 34, pp. 167–76.
15. N. Abedrabbo, F. Pourboghrat, and J. Carsley: *Int. J. Plast.*, 2006, vol. 22, pp. 314–41.
16. Deutsche-Gesellschaft-für-Metallkunde: *Atlas der Warmformgebungseigenschaften von Nichteisenmetallen: Aluminiumwerkstoffe*, Aluminium-Verlag, Oberursel, Germany, 1978.
17. Q. Zhao: Doctoral Thesis, Norwegian University of Science and Technology, Trondheim, Norway, 2013.
18. W.F. Hosford and J.L. Duncan: *J. Met.*, 1999, vol. 51, pp. 39–44.
19. Y. Bergstrom: *Mater. Sci. Eng.*, 1970, vol. 5, pp. 193–200.
20. F.J. Humphreys and M. Hatherly: *Recrystallization and Related Annealing Phenomena*, Elsevier, Oxford, U.K., 2004.
21. Y. Bergstrom, Y. Granbom, and D. Sterkenburg: *J. Metall.*, 2010, article ID 647198, pp. 1–16.
22. K. Bång: M. Sc. Thesis, Royal Institute of Technology, Stockholm. Sweden, 2011.
23. H.-E. Ekström, Unpublished research, 2003.
24. J. Kohout: *Fatigue Fract. Eng. Mater. Struct.*, 2000, vol. 23, pp. 969–77.
25. P. Juijerm and I. Altenberger: *Scripta Mater.*, 2006, vol. 55, pp. 943–46.
26. T. Saito, S. Muraishi, C.D. Marioara, and R. Holmestad: *13th International Conference on Aluminium Alloys*, 2012.
27. J. Kanesund and S. Johansson: *13th International Conference on Aluminium Alloys*, 2012.
28. K. Teichmann, C.D. Marioara, K.O. Pedersen, and K. Marthinsen: *Mater. Sci. Eng. A*, 2013, vol. 565, pp. 228–35.
29. R.I. Stephens, A. Fatemi, R.R. Stephens, and H.O. Fuchs: *Metal Fatigue in Engineering*, John Wiley & Sons, New York, U.S.A., 2001.
30. P. Juijerm, U. Noster, I. Altenberger, and B. Scholtes: *Mater. Sci. Eng. A*, 2004, vol. 379, pp. 286–92.
31. F.R. Larson and J.A. Miller: *Trans. ASME*, 1952, vol. 74, pp. 765–75.
32. A.K. Mukherjee, J.E. Bird, and J.E. Dorn: *Trans. Am. Soc. Met.*, 1969, vol. 62, pp. 155–79.
33. E. Nes: *Scripta Metall. Mater.*, 1995, vol. 33, pp. 225–31.
34. A.K. Mukherjee: *Mater. Sci. Eng. A*, 2002, vol. 322, pp. 1–22.
35. F.C. Monkman and N.J. Grant: *Proc. ASTM*, 1956, vol. 56, pp. 593–620.
36. J.G. Kaufman: *Properties of Aluminum Alloys: Tensile, Creep, and Fatigue Data at High and Low Temperatures*, ASM International, Materials Park, OH, U.S.A, 1999.
37. L.F. Mondolfo: *Aluminium Alloys: Structure and Properties*, Butter Worths, London, U.K., 1976.
38. Y. Du, Y.A. Chang, B.Y. Huang, W.P. Gong, Z.P. Jin, H.H. Xu, Z.H. Yuan, Y. Liu, Y.H. He, and F.Y. Xie: *Mater. Sci. Eng. A*, 2003, vol. 363, pp. 140–51.
39. Q. Zhao, B. Holmedal, and Y. Li: *Philos. Mag.*, 2013, DOI: 10.1080/14786435.2013.794315, pp. 1–17.
40. W.L. Bradley, D.K. Matlock, and W. Nam: *Metall. Trans. A*, 1976, vol. 7A, pp. 425–30.
41. D.H. Shin and S.W. Nam: *J. Korean Inst. Met.*, 1983, vol. 21, pp. 628–34.
42. Z.A. Yang and Z.G. Wang: *Mater. Sci. Eng. A*, 1991, vol. 142, pp. 25–33.
43. Z.A. Yang, Z. Wang, X. Hu, and Z. Wang: *Acta Metall. Mater.*, 1993, vol. 41, pp. 933–40.
44. D.K. Shetty and M. Meshii: *Metall. Trans. A*, 1975, vol. 6, pp. 349–58.
45. N.E. Dowling, C.A. Calhoun, and A. Arcari: *Fatigue Fract. Eng. Mater. Struct.*, 2009, vol. 32, pp. 163–79.